Supplementary Information

Simultaneous Dual-Raman-Shift Scanning-Free Stimulated Raman Scattering Microscopy for Label-Free Biomolecular Imaging

Binglin Shen[1], Zhi Zeng[1], Haiyang Li[1], Zongyi Yin[2], Jiazi Yu[3], Zhenglin Li[1], Chao Zhang[1], Yide Zhang[4], Rui Hu[1], Junle Qu[1], Liwei Liu[1*]

[1]*Key Laboratory of Optoelectronic Devices and Systems of Guangdong Province and Ministry of Education, College of Physics and Optoelectronic Engineering, Shenzhen University, Shenzhen 518060, China.*

[2]*Department of Hepatobiliary Surgery, Shenzhen University General Hospital, Shenzhen 518055, China.*

[3]*Department of Colorectal Surgery, Ningbo Medical Center Lihuii Hospital, Ningbo 315100, China.*

[4]*Department of Electrical, Computer, and Energy Engineering, Biomedical Engineering Program, University of Colorado Boulder, Boulder, CO 80309, USA.*

Contents

Supplementary Note 1 Non-co-path dual-color SRS

For spectral focusing SRS systems[1-3], the reported dual-color imaging uses two PBSs for optical separation, and two precise displacement stages for adjusting time delay of the pump light and Stokes light with different polarizations, which respectively match the conditions of two molecular resonances[4]. However, this approach increases optical path complexity, equipment costs, and space requirements.

Different from the co-path SDRSRS system in the main text, we also proposed non-co-path dual-color SRS imaging that leverages the different refractive indices of light at different wavelengths through a PBS (Supplementary Fig. 1a). The dispersion formula for N-SF1 glass (the material of PBS) is given by

$$n^2 - 1 = \frac{1.60865158\lambda^2}{\lambda^2 - 0.0119654879} + \frac{0.23775916\lambda^2}{\lambda^2 - 0.0590589722} + \frac{1.51530653\lambda^2}{\lambda^2 - 135.521676} \quad (1)$$

For pump light at 800 nm and Stokes light at 1040 nm, the refractive index difference in N-SF1 is approximately δn = 0.008. In our polarization separation and dual-phase modulation optical path, vertically polarized excitation lights, $E_{p,H}(t)$ and $E_{s,H}(t)$, travels 2.54 cm farther than horizontally polarized lights, $E_{p,V}(t + \Delta t_1)$ and $E_{s,V}(t + \Delta t_2)$, in the one-inch PBS (Supplementary Fig. 1a). Assuming the OPD between $E_{p,H}(t)$ and $E_{s,H}(t)$ is 0, the OPD between $E_{p,V}(t + \Delta t_1)$ and $E_{s,V}(t + \Delta t_2)$ is $\delta n \delta l$ = 0.008 × 25.4 mm ≈ 0.2 mm, with a difference wavenumber, $\Delta\Omega$ of 72 cm^{-1} (0.36 cm^{-1}/μm).

When the time-delay displacement stage is adjusted so that $E_{p,H}(t)$ and $E_{s,H}(t)$ match the resonance of protein molecules (2930 cm^{-1}), naturally, $E_{p,V}(t + \Delta t_1)$ and $E_{s,V}(t + \Delta t_2)$ precisely match the resonance of lipid molecules (2858 cm^{-1})[5-12]. We measured the wavenumber deviation between the two excitation paths was approximately 80 cm^{-1} (Supplementary Fig. 1b). As contrast, in another optical path scheme (Supplementary Fig. 1c), where horizontally and vertically polarized excitation light travel the same path through the PBS, the orthogonal demodulated SRL signal could only match a single wavenumber (Supplementary Fig. 1d).

Nevertheless, in our practice, the non-co-path dual-color SRS configuration has a difference in the beam quality of the two polarization paths, and balanced detection is hardly achieved. The imaging quality of the dual channel is not as good as that of the co-path SDRSRS system.

Supplementary Note 2 Polyploid giant cancer cell imaging

We imaged lipid droplet distribution in polyploid giant cancer cells[13-15] to visualize intracellular lipid droplet transport at the subcellular scale[16] (Supplementary Fig. 3a), observing changes in CH_3 and CH_2 content. The evolution of relative lipid droplet content in ROI1 (Supplementary Fig. 3b) and ROI2 (Supplementary Fig. 3c) over time reveals the dynamic process of lipid droplet transfer between regions[17]. This lipid droplet enrichment may be closely related to cancer cell malignancy. In more malignant cancer cells, lipid droplet accumulation is more pronounced, and lipid droplet transfer occurs more rapidly.

We also analyzed lipid droplet changes in polyploid giant cancer cells over extended periods. SDRSRS imaging of these cells (Supplementary Fig. 3a) clearly demonstrates the dynamic changes of lipid droplets at cell edges, showing transfer from one position to another. These changes exhibit quantifiable characteristics (Supplementary Fig. 3b,c). The zoom-in views (Supplementary Fig. 3d) more clearly show the disappearance and enrichment of lipid droplets, allowing direct observation of lipid droplet dynamics within cells. Abnormal lipid droplet changes in polyploid giant cancer cells may be related to malignant proliferation and metastatic abilities. The disappearance of lipid droplets may result from increased lipid utilization to meet demands for rapid growth and proliferation. Conversely, lipid droplet enrichment may occur as cells store excess lipids under specific physiological conditions, such as nutritional deficiency or oxidative stress, to maintain cellular survival and function. Further research into these lipid droplet dynamics may provide new therapeutic targets for cancer treatment, such as regulating intracellular lipid metabolism to inhibit cancer cell growth and metastasis.

Supplementary Note 3 Two-cell imaging

The two-cell observation (Supplementary Fig. 4a) revealed the directional lipid droplet “waves”. Under specific physiological conditions in cancer cells, an inherent regulatory mechanism likely guides lipid droplets toward regions more conducive to cell growth and proliferation. During bidirectional lipid droplet transfer (Supplementary Fig. 4b), the cellular microenvironment surrounding the lipid droplets undergoes corresponding changes. This microenvironment, including various organelles, cytoskeletal components, and signaling molecules, plays a crucial role in this process. For example, the cytoskeleton provides a structural framework for lipid droplet movement, and changes in its organization and dynamics can either facilitate or impede lipid droplet transfer. Signaling molecules, such as specific kinases and phosphatases, may also regulate interactions between lipid droplets and other cellular components, influencing the direction of lipid droplet movement.

Previous studies have shown that regulating lipid droplet movement and enrichment can inhibit cancer cell growth and proliferation. For instance, inhibiting specific proteins involved in lipid droplet dynamics can significantly reduce cancer cell viability and tumor growth[18]. Similarly, other studies have found that altering lipid droplet composition may disrupt normal movement patterns and impair cancer cell metastasis[19-21].

These findings indicate that lipid droplets are not merely passive storage organelles but actively participate in regulating cancer cell behavior. The directional movement of lipid droplets may relate to cellular requirements for distributing lipids and related molecules to specific regions for membrane synthesis, energy production, or signal transduction for cancer cell survival and progression.

Supplementary Note 4 Descriptive statistics of component ratio

Drug molecules may affect key regulatory factors governing lipid droplet transfer, potentially blocking abnormal lipid droplet movement. Analysis of lipid component ratios (Fig. 4e) across four groups (normal, cancer, CRT, PDT) revealed: normal tissues had a ratio of 0.34 ± 0.19, cancer tissues 0.18 ± 0.13, CRT tissues 0.32 ± 0.18, and PDT tissues 0.38 ± 0.10. We found that cancer tissues had significantly lower average component ratios than normal tissues, while CRT and PDT showed ratios approaching those of normal tissues. This comparison suggests significant component ratio changes in cancer tissues, with PDT treatment potentially helping restore ratios to near-normal levels.

Our analysis of relative frequency distribution of ratio (Supplementary Fig. 6b) shows that component ratios in normal tissues primarily ranged between 0.2 and 0.4, while cancer tissues showed a significant shift toward lower values (0.1—0.25). The distribution of CRT resembled normal tissues but with a slightly lower peak value and wider distribution range. In contrast, PDT showed a more concentrated distribution with peaks between 0.35 and 0.45, indicating relatively high component ratios. This further confirms that cancer tissues exhibit significantly reduced component ratios, with PDT treatment potentially restoring ratios to near-normal levels. CRT treatment effects approximated normal tissues but with more dispersed data distribution.

The AUC values between each pair of sample data from the four groups (Fig. 4f) ranged from 0.5 to 0.9, reflecting varying abilities to distinguish between cancer patients and normal controls or different treatment groups. Pre-treatment AUC values (0.75 ± 0.03) differed significantly from the normal control group. Post-treatment AUCs were 0.54 ± 0.03 (CCR8) and 0.56 ± 0.03 (PD1), indicating insufficient differentiation from normal tissues. The two treatment groups showed higher AUC values (0.72 ± 0.03 and 0.87 ± 0.02) compared to the cancer group, indicating significant differences between patients before and after treatments, potentially indicating immunotherapy efficacy.

Supplementary Note 5 Classification analysis

We used PCA to classify different tissue types (Fig. 4g). The dots represent projections of different samples onto two principal components, PCA1 and PCA2. Although sample distributions across different tissues (normal, cancer, CRT, PDT) show some overlap, distinct separation trends are observable. Notably, cancer samples (marked in red) display different distributions on PCA1 and PCA2 compared to other tissue samples. PCA1 and PCA2 explained 73.2% and 26.8% of total variance, respectively, indicating major role of PCA1 in explaining data variability.

However, PCA has well-known limitations, most notably its restriction to linear combinations of original data. UMAP represents one alternative method for non-linear dimensionality reduction based on topological data analysis approaches.We employed UMAP clustering to segment normal, cancer, CRT, PDT tissues (Fig. 4h). Cancer and normal tissues are clearly distinguished in the spatial distribution. The clustering regions help distinguish cancer and treated tissues, indicating effective immunotherapy with PDT.

Supplementary Note 6 K-means analysis of human colorectal cancer

The k-means classification result for human colorectal cancer tissues (red dots) and paracancerous tissues (blue dots) based on component ratios is shown in Supplementary Fig. 7b. While the two tissue types show some distinction in two-dimensional space, they are not completely separated. Classification boundaries (dotted lines) reveal mixing of some cancer and paracancerous tissues near these boundaries, indicating certain overlapping characteristics between these tissue types.

Dependence of scores for cancer tissues (red) and paracancerous tissues (blue) on observed values is shown in Supplementary Fig. 7c. Generally, paracancerous tissue scores were higher than cancer tissue scores. Both curves show considerable fluctuation, but paracancerous tissues demonstrate significantly higher average scores and fluctuation ranges. Dotted lines represent average scores for each tissue type, clearly showing higher average scores for paracancerous tissues. This difference may reflect distinct biological characteristics or molecular expression patterns between the two tissue types.

Supplementary Note 7 Collinear balanced detection

Due to the birefringence effect on the pump and Stokes beams in the BFC, they were divided into two time-separated paths: horizontal polarization and vertical polarization. Before detection, the pump beams with orthogonal polarization were spatially separated by the WP. At this point, the phase difference of the SRL carried by the pump beams of the two polarizations was π. Using LIA for differential operation allowed us to adjust the phase difference between the pump beams of the two polarizations to 0, enhancing the signal by a factor of 2. While noise increased by the square root of two, the overall signal was enhanced. Notably, this method effectively suppressed the relative intensity noise (RIN) of the laser.

Thereby, we naturally achieved collinear balanced detection, enabling subtraction of common-mode noise in the electronic domain (Supplementary Fig. 8a). This configuration exploits the fact that both orthogonally polarized pump components share the same optical path and experience identical laser-intensity fluctuations, allowing their differential detection to suppress RIN without requiring dual-beam alignment or matched reference arms.

To quantitatively assess noise suppression, we recorded ten consecutive SRS spectra at demodulation times of 4 μs (Supplementary Fig. 8b) and 1 μs (Supplementary Fig. 8c). Each spectrum acquired with 10 ms total integration time was treated as a high-SNR approximation to the noise-free Raman response and used as the reference for estimating per-spectrum noise levels. For each of the ten spectra, the SNR was computed before and after balanced-detection processing. The balanced-detection configuration yielded a mean SNR improvement of 11 dB, arising from both higher effective energy utilization and robust rejection of correlated electronic and RIN fluctuations.

In contrast to traditional optical balanced-detection schemes that require precise phase matching between a sample arm and an external reference arm, which often necessitate active stabilization or additional optical hardware. Our approach achieves phase matching intrinsically because the two polarization channels originate from the same modulated Stokes beam and propagate through the exact same optical and electronic pathways. This collinearity eliminates drift-prone differential phase errors and substantially improves experimental robustness, especially during long acquisitions or when imaging turbid biological tissues.

Importantly, the collinear balanced-detection module also preserves the ability to demodulate two Raman frequency shifts (Ω_1 and Ω_2) simultaneously, although it does not separate them chemically at the detection stage. Instead, Ω_1 and Ω_2 separation occurs upstream via the birefringent-crystal-induced OPD. The resulting dual-channel demodulated signals thus reflect two vibrational resonances obtained under identical excitation and noise environments with improved SNR.

We performed imaging on living cells using the collinear balanced detection mode (Supplementary

Fig. 9). We clearly observed dynamic lipid droplet movement in a cell. Initially located at the cell membrane, these lipid droplets gradually moved and mergied with larger lipid droplets. Furthermore, we observed lipid droplets transferred between two contacting cells, suggesting that lipid droplets may play an important role in intercellular communication and material transfer. These processes visually demonstrate lipid droplet dynamics and interactions within cells and between cells, providing experimental evidence for understanding cellular lipid metabolism and transport mechanisms.

Supplementary Note 8 Compatibility with other imaging modalities

Although SRS, two-photon autofluorescence (TPAF), and second harmonic generation (SHG) are all nonlinear optical imaging modalities, SRS has certain practical limitations. Specifically, SRS typically requires spectral scanning to obtain comprehensive Raman information, making it difficult to integrate with other real-time imaging methods. This spectral scanning process not only increases acquisition time for other imaging modalities, reducing overall efficiency, but also introduces problems such as phototoxicity and photobleaching. Phototoxicity can damage biological samples and affect normal cellular physiological functions, while photobleaching reduces fluorescence signal intensity and degrades image quality. Additionally, spectral scanning may generate thermal effects, causing further sample damage.

In contrast, SDRSRS imaging has compatibility with other imaging modes. The imaging time (~0.26 sec@512×512) aligns with TPAF and SHG, eliminating the need for Raman spectral scanning during multimodal imaging. We conducted multiplex optical imaging on human colorectal cancer tissues using different modalities: SRS 2930 cm^{-1}, SRS 2850 cm^{-1}, TPAF, and SHG as shown in Supplementary Fig. 10.

In the SRS images, we clearly observed different chemical component distributions within tumor tissue. The molecular vibration characteristics (2930 cm^{-1} and 2850 cm^{-1}) provide detailed information about tissue chemical composition. SRS imaging at different Raman shifts help understand the content and distribution of biological macromolecules such as lipids and proteins in tumor tissues.

TPAF imaging reveals endogenous fluorescence in tumor tissues. Endogenous fluorescent substances like tryptophan and riboflavin emit fluorescence under two-photon excitation. These fluorescence signals can reveal cellular metabolic states and biomolecule distribution[22, 23]. Tumor cell morphology and distribution and intracellular biomolecules can be observedx.

SHG imaging captures nonlinear optical phenomena in tissues. SHG signals typically originate from molecules with non-centrosymmetric structures, such as collagen. Collagen distribution and arrangement change in tumor tissues, and SHG imaging clearly displays these changes, helping us understand tumor tissue structure and fibrosis degree[23, 24].

By comprehensively analyzing these multimodal images, we gain a more complete understanding of tumor tissue structure and composition. Each imaging moadlity provides complementary information—from chemical composition to cell morphology, from molecular distribution to tissue structure—presenting a comprehensive visualization of tumor tissues.

Supplementary Note 9 Long-term stability characterization

To quantitatively evaluate long-term system stability, we monitored the relative phase, Raman-shift separation $\Delta\Omega$, and signal intensity of both demodulated channels during continuous operation over a 2-hour period. Measurements were performed under standard laboratory conditions without active environmental stabilization. The relative phase deviation between the two channels remained below 0.5 °, while the normalized signal intensity exhibited <2% fluctuation over the entire duration. No measurable drift in $\Delta\Omega$ was observed, confirming the stability of the birefringent-crystal-induced OPD. These results demonstrate that SDRSRS is intrinsically phase-locked and robust against long-term drift.

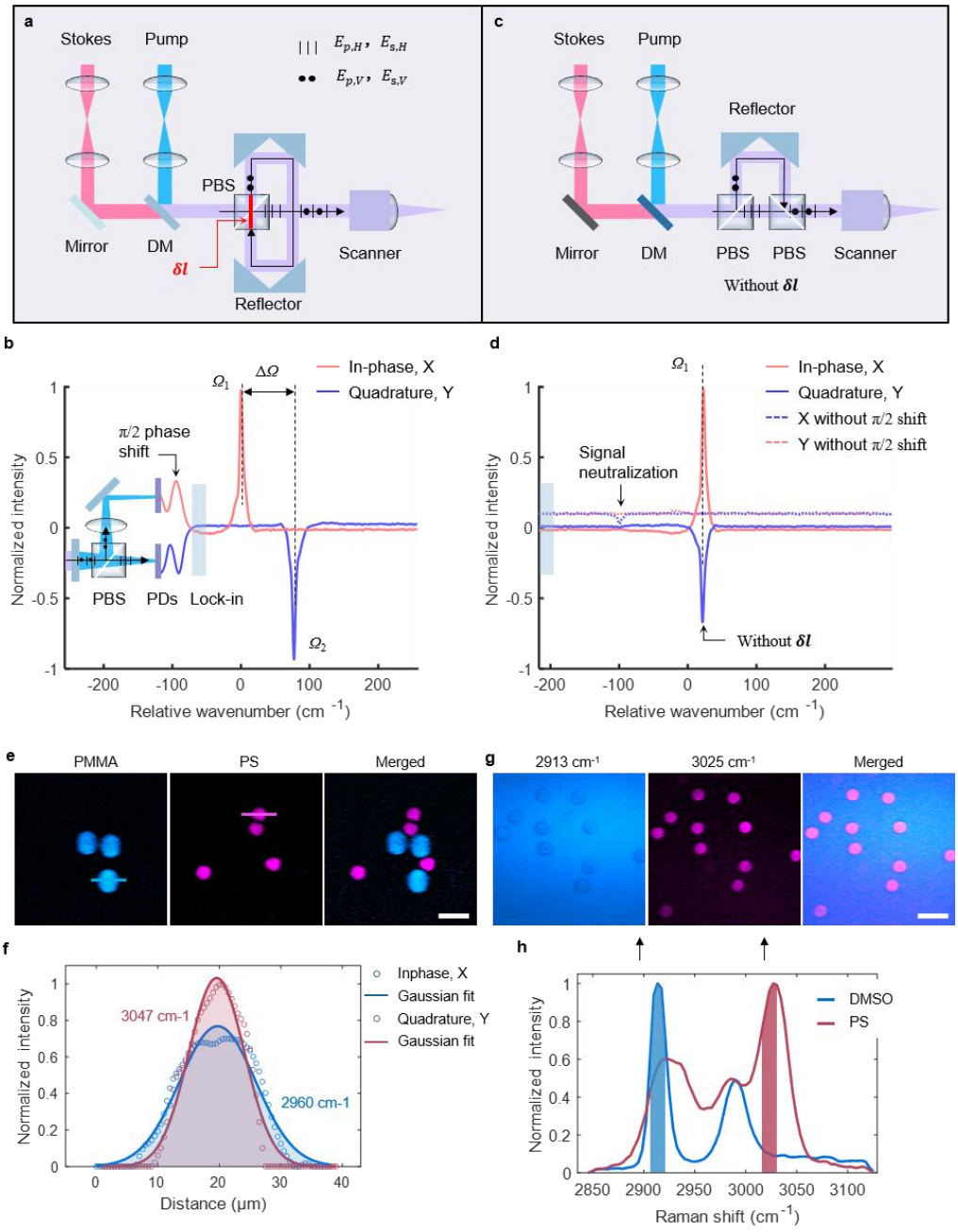

Supplementary Fig. 1 Non-co-path dual-color SRS.

(a) Dual-color SRS imaging leveraging the different refractive indices of light at different wavelengths through a PBS, which is different from the reported method[4] and our method in the main text. **(b)** Raman spectral scanning with orthogonal demodulated dual-Raman-shift in non-co-path dual-color SRS. **(c)** Another optical path scheme, where horizontally and vertically polarized excitation light travel the same path through the PBS. **(d)** The orthogonal demodulated SRL signal could only match a single wavenumber without δl (no dual Raman shift). Furthermore, the X and Y signal is neutralized when π/2 shift is not applied. **(e)** Simultaneous SRS images of PMMA and PS beads using the method in **(a)**. **(f)** Intensity profiles along the solid line in **(e)**. **(g)** Simultaneous SRS images of DMSO and PS at Raman shift coordinates shown in **(h)**. Scale bars, 20 μm.

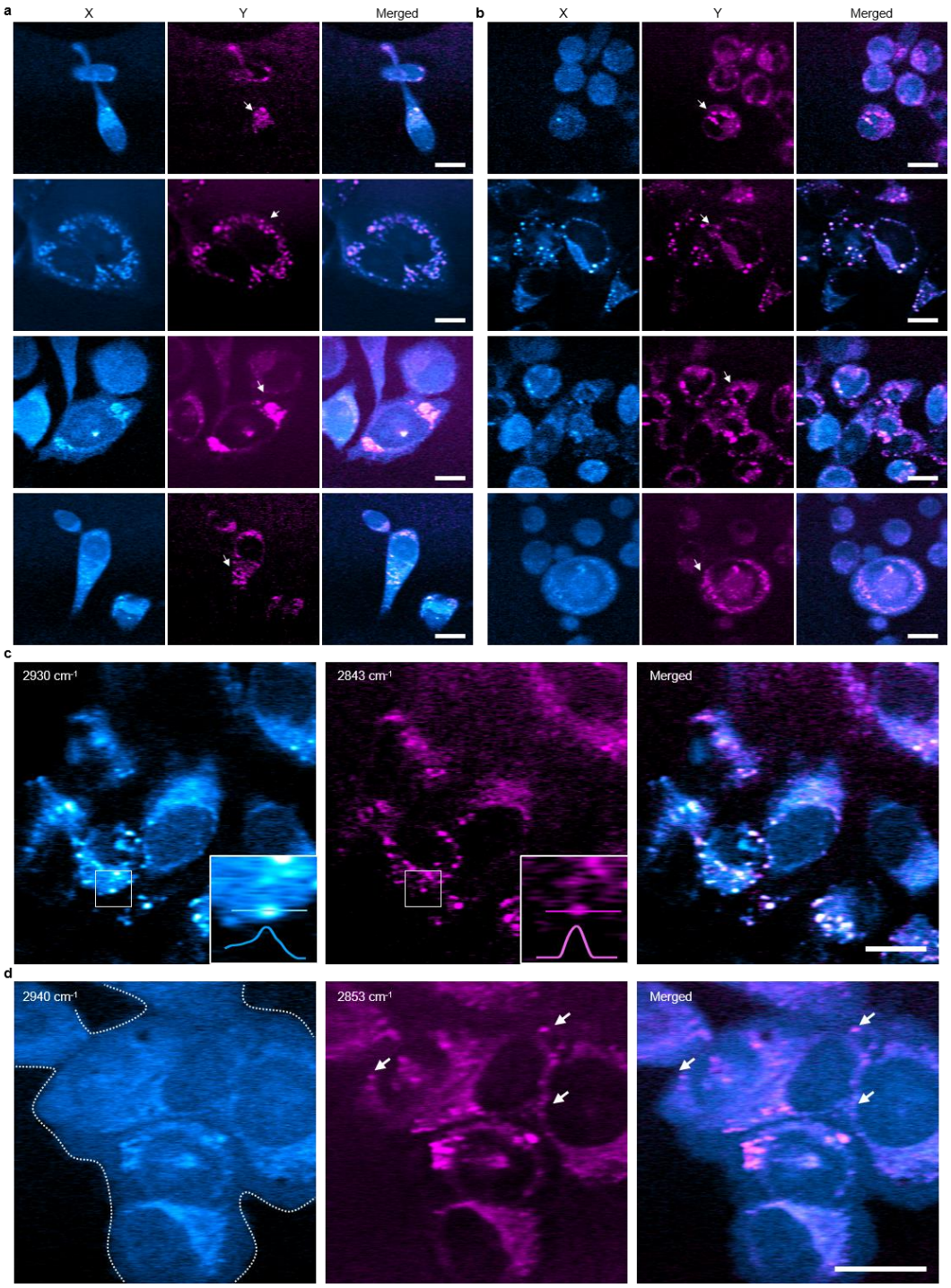

Supplementary Fig. 2 Label-free SDRSRS images of living cells.

(a) SDRSRS images of living cells at the simultaneous collection of Raman shifts of 2940 cm^{-1} and 2853 cm^{-1}. **(b)** SDRSRS images of living cells at the simultaneous collection of Raman shifts of 2930 cm^{-1} and 2843 cm^{-1}. White arrows indicate lipids. **(c)** Images of lipid-rich cells at Raman shifts of 2930 cm^{-1} and 2843 cm^{-1}. Blue and red solid lines in the images indicate the cross-sectional lines shown. **(d)** Close-up images of giant cancer cells at Raman shifts of 2940 cm^{-1} and 2853 cm^{-1}. Cell outlines are delineated by white dashed lines. Cell imaging experiments were independently repeated across at least four cultures with consistent results. Scale bars: 20 μm.

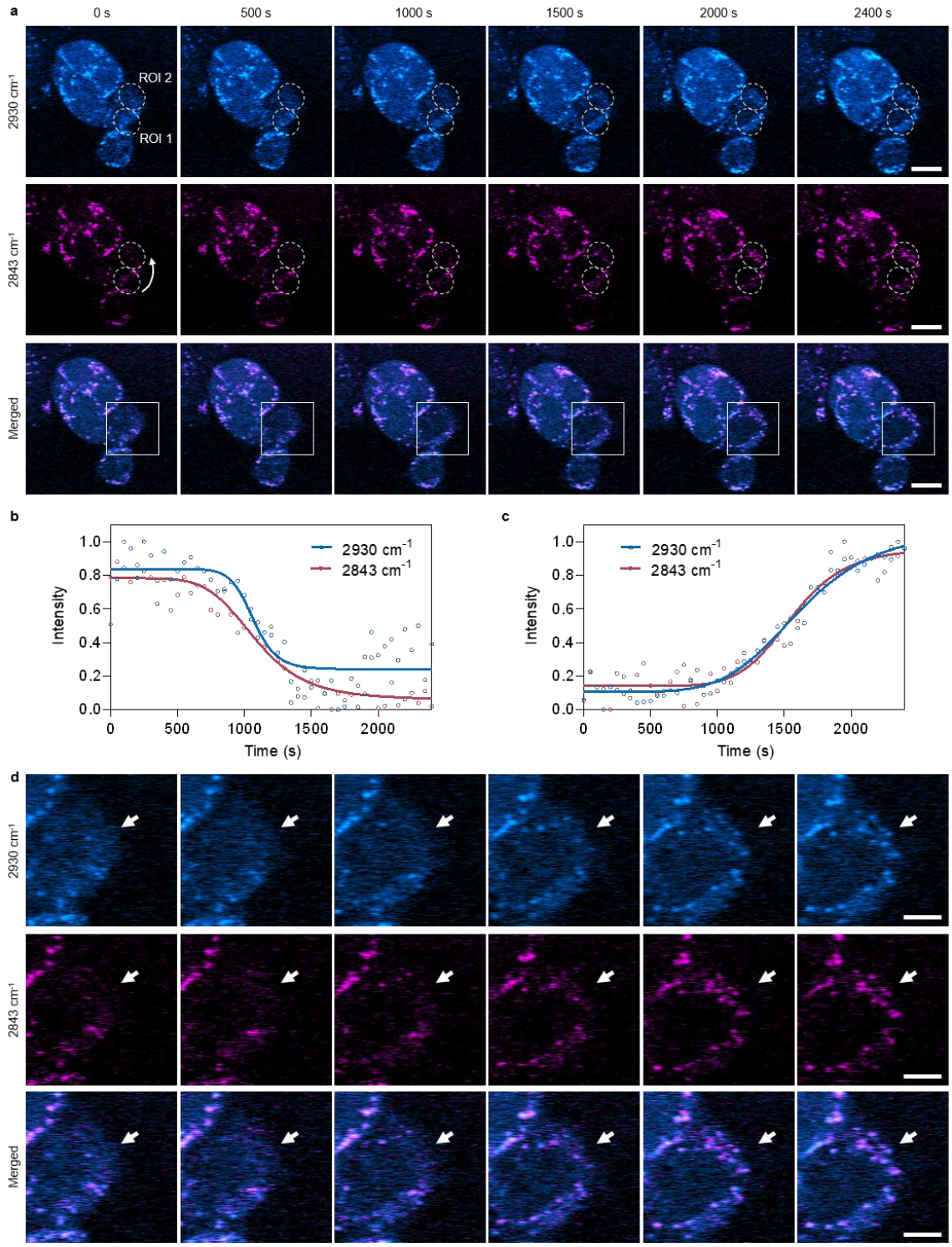

Supplementary Fig. 3 SDRSRS images of polyploid giant cancer cells.

(a) Time-lapse images of polyploid giant cancer cells. Lipid droplet transfers fromROI1 to ROI2. Variation of 2930 cm^{-1} and 2843 cm^{-1} intensities over time at the ROI1 **(b)** and ROI2 **(c)**. **(d)** corresponds to magnified view of the boxed regions in **(a)**. White arrows indicate lipid dynamics. Scale bars: 20 μm in **(a)** and 10 μm in **(d)**.

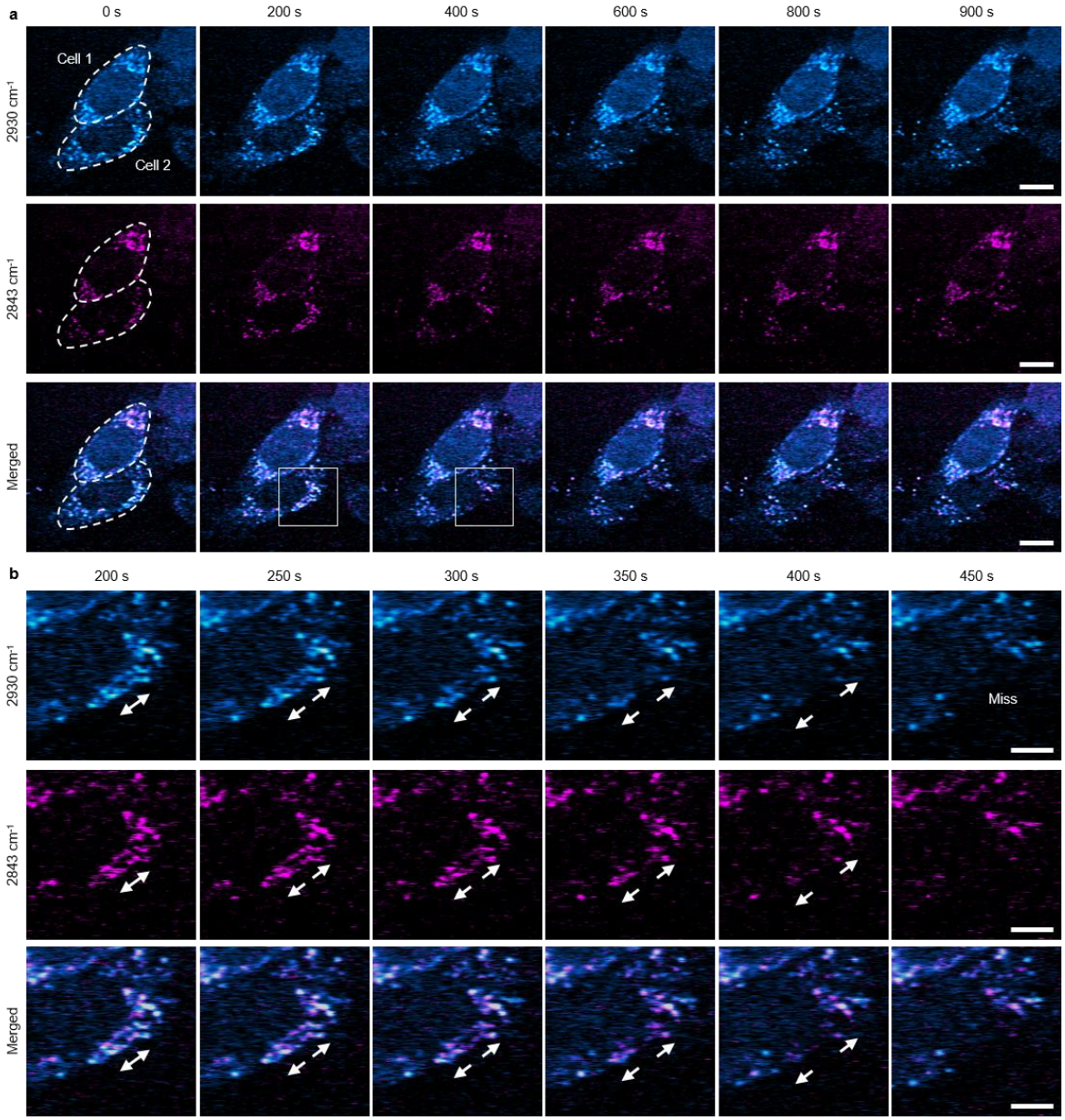

Supplementary Fig. 4 SDRSRS images of living Hela cells.

(a) Time-lapse images of living Hela cells. Lipid droplet transfers fromROI1 to ROI2. Cell outlines are delineated by white dashed lines. **(b)** corresponds to magnified view of the boxed regions in **(a)**. White arrows indicate lipid wave. Scale bars: 20 μm in **(a)** and 10 μm in **(b)**.

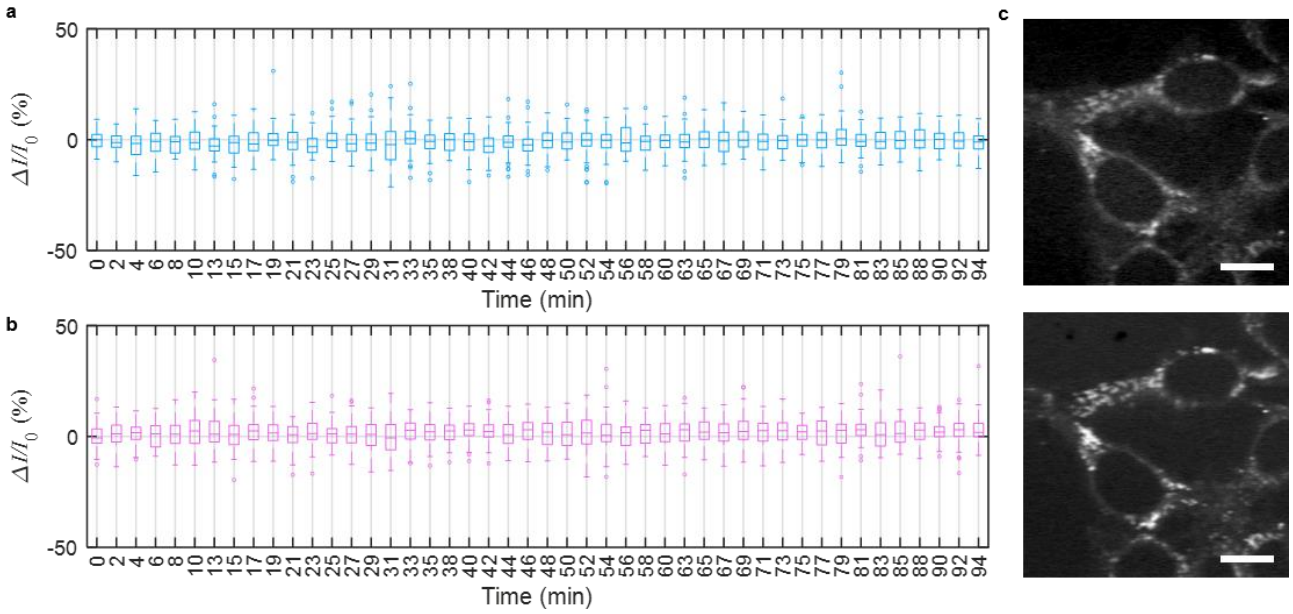

Supplementary Fig. 5 Stability verification of imaging intensity varying with time.
Time variation of CH_3 **(a)** and CH_2 **(b)** intensities (n = 50). No weakening of the SRS signal was observed. **(c)** Cell images at the beginning (top panel) and end (bottom panel) time point with consistent intensiy. Scale bars: 20 μm.

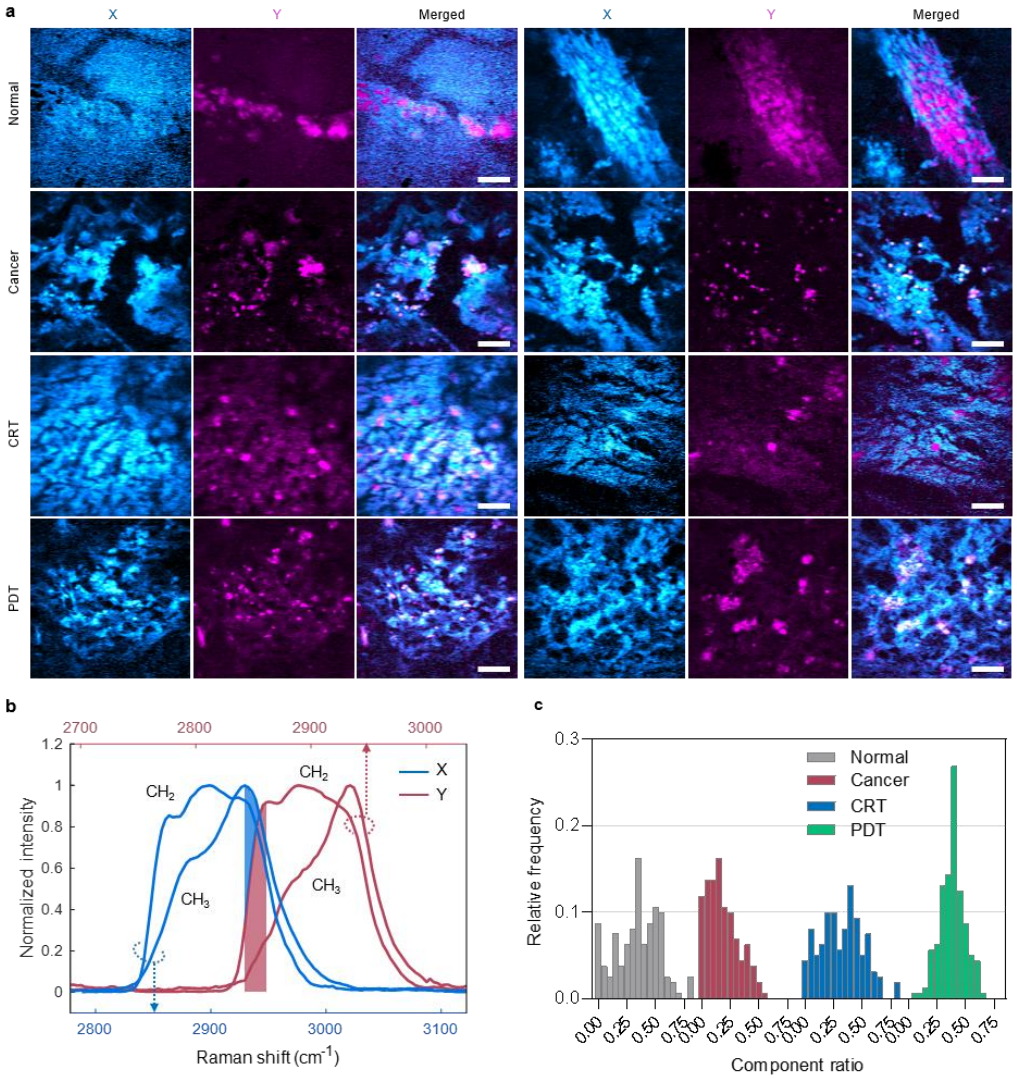

Supplementary Fig. 6 SDRSRS analyses of mouse liver cancers.
(**a**) Simultaneous 2930 cm^{-1} (X) and 2843 cm^{-1} (Y) images of normal liver, liver cancer, CRT, and PDT tissues. **(b)** Dual-SRS spectra of liver tissue. Overlapping blue and red bars represent the simultaneously acquired Raman shift coordinates. **(c)** The relative frequency distribution of component ratios for the normal, cancer, CRT, and PDT samples (n = 160). Scale bars: 20 μm.

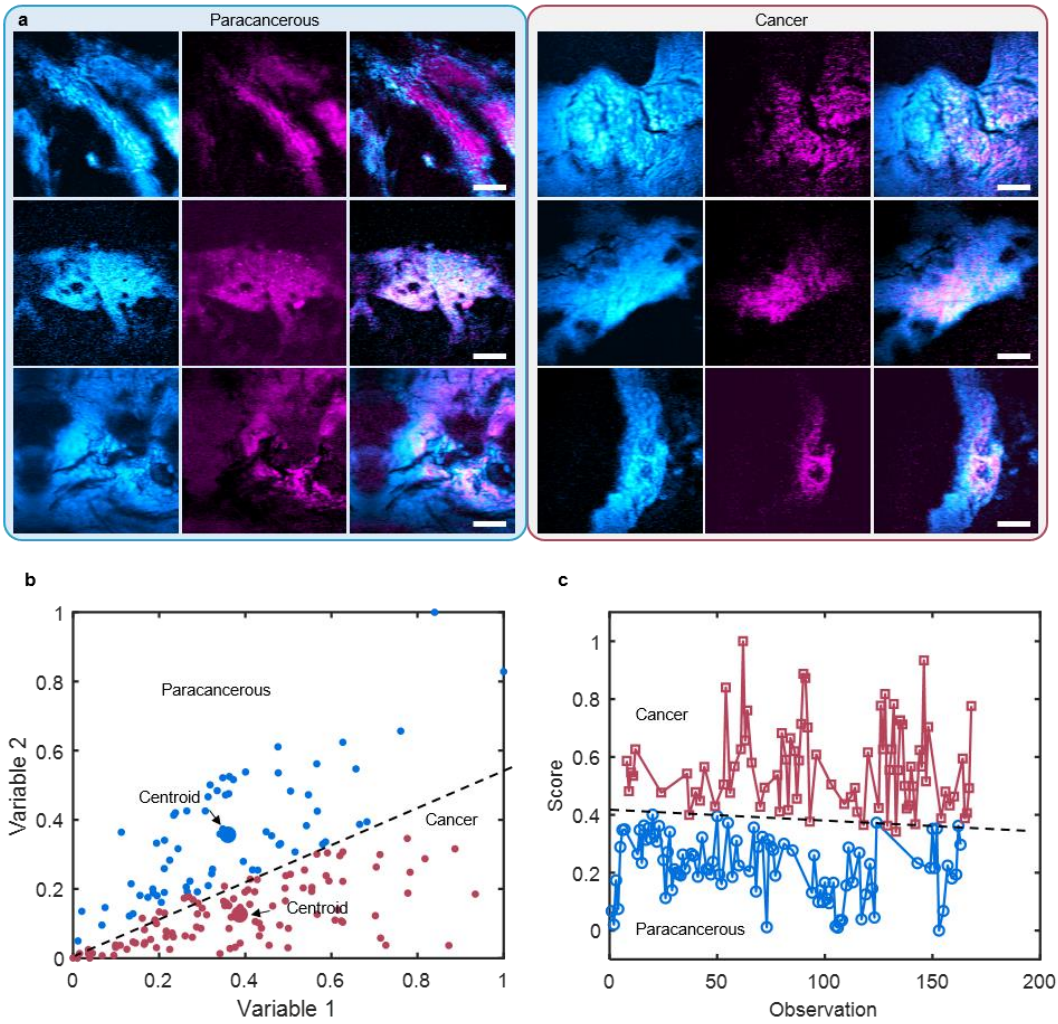

Supplementary Fig. 7 SDRSRS analyses of human colorectal cancers.

(**a**) Simultaneous 2930 cm^{-1} (X) and 2843 cm^{-1} (Y) images of colorectal paracancerous (left) and cancer (right) samples. (**b**) The k-means clustering of the paracancerous and cancer samples (n = 84). (**c**) Dependence of scores for cancer tissues (red) and paracancerous tissues (blue) on observed values using k-means (n = 84). Scale bars: 20 μm.

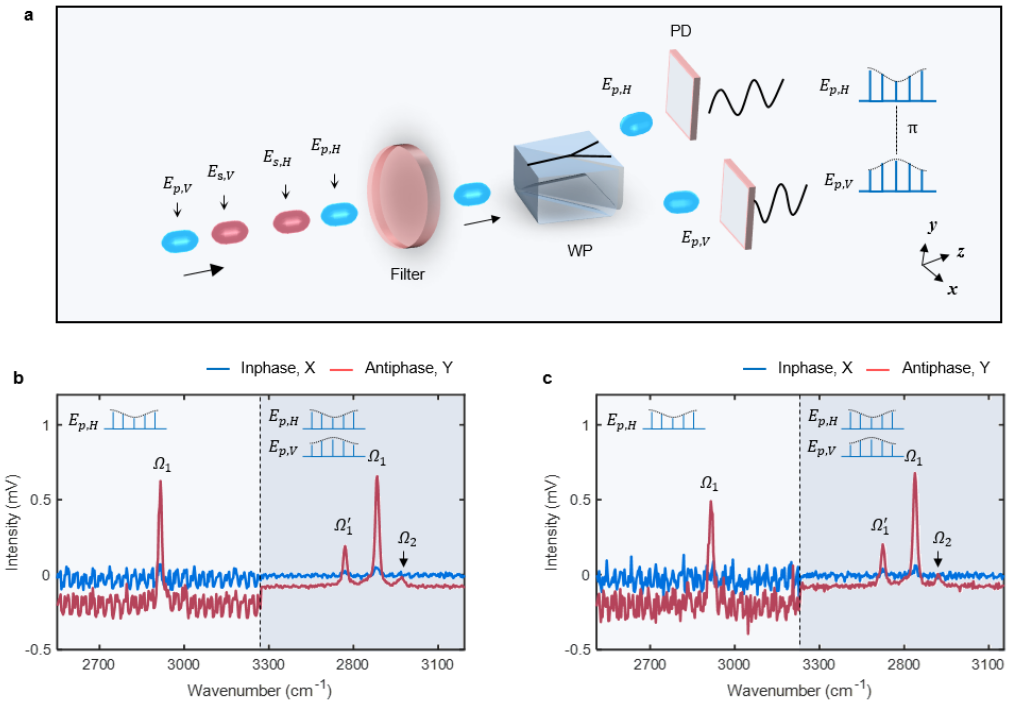

Supplementary Fig. 8 Collinear balanced detection.

(a) Collinear balanced detection mode by adjusting phase values of dual channels in the detection module (e.g., setting to π). Comparison of Raman spectra using collinear balanced detection and without collinear balanced detection at a demodulation time of 4 μs **(b)** and 1 μs **(c)**.

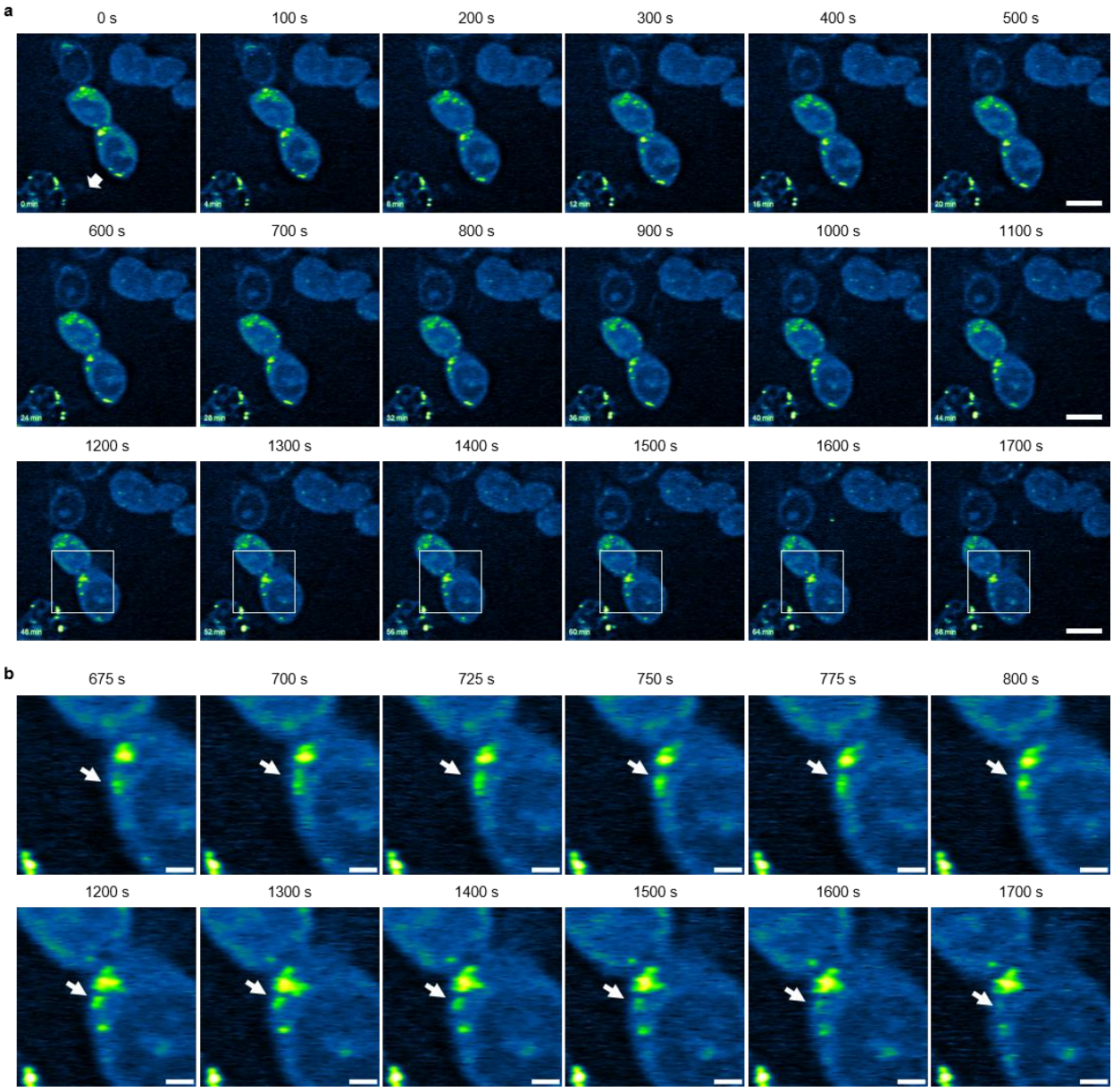

Supplementary Fig. 9 SRS images of living cells with the collinear balanced detection.
(**a**) Time-lapse images of living cells. The blue pseudo-color represents CH_3 and the green pseudo-color represents CH_2. (**b**) Zoom-in views of the boxed regions in **(a)** showing dynamic lipid droplet movement in the cell. White arrows indicate lipid dynamics. Cell outlines are delineated by white dashed lines. Imaging was independently repeated across at least four cultures with consistent results. Scale bar, 20 μm in **(a)** and 5 μm in **(b)**.

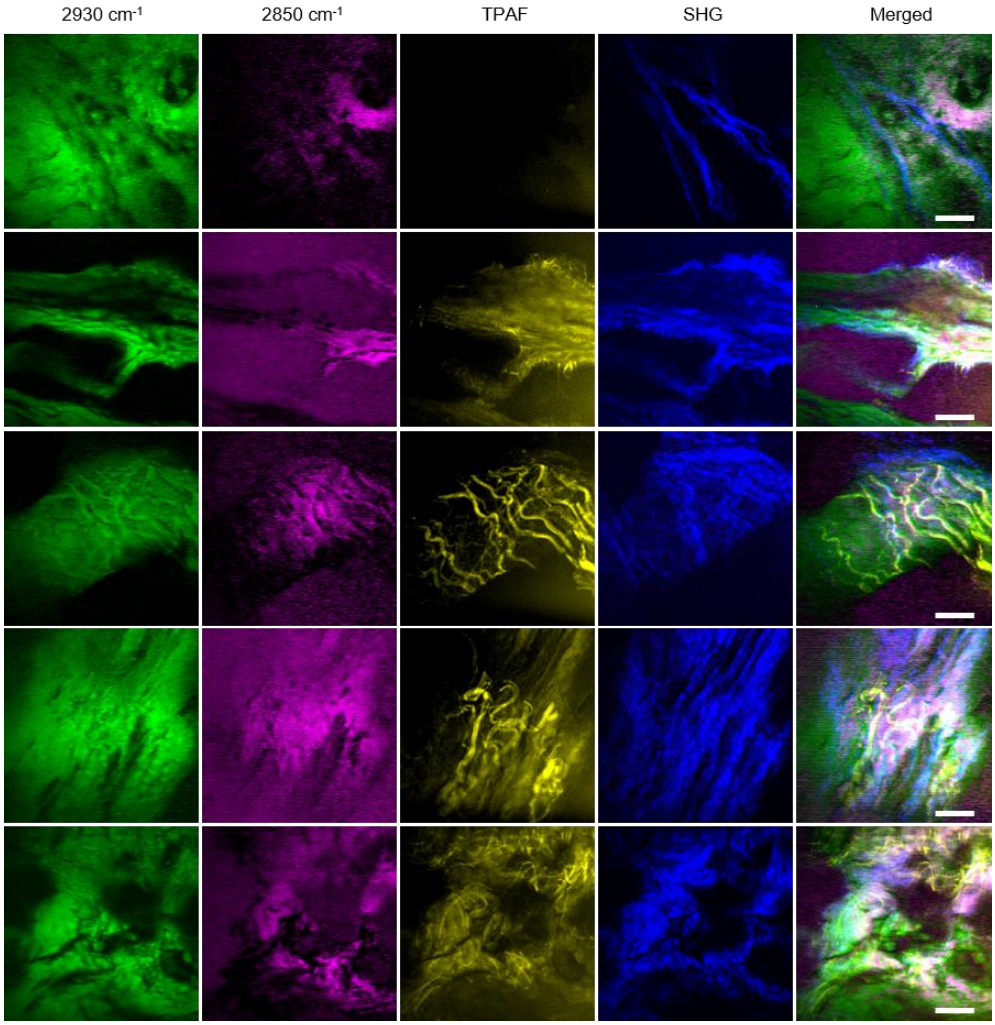

Supplementary Fig. 10 Simultaneous collection of multimodal optical images.
Multimodal optical images of human colorectal cancer tissues include: SRS 2930 cm^{-1}, SRS 2850 cm^{-1}, TPAF, and SHG. Experiments were independently performed across biological replicates (n = 5 mice). Scale bars: 20 μm.

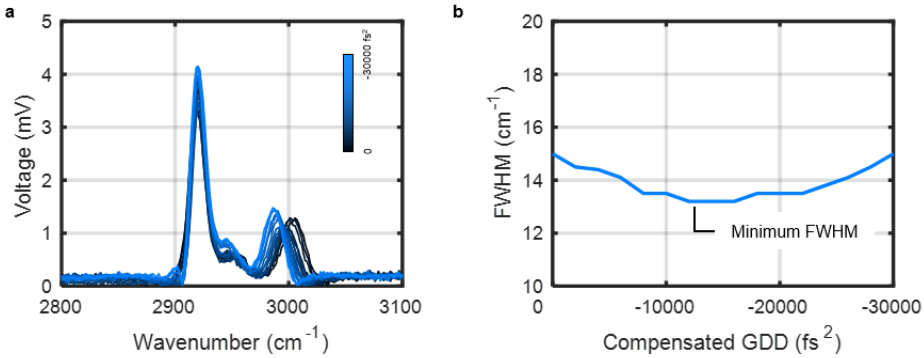

Supplementary Fig. 11 GDD compensation and SRS spectral resolution.
(**a**) SRS spectra under different GDD compensation in the pump beam to search the consistent linear chirp parameter β (n = 16). (**b**) SRS spectral FWHM at different compensated GDD.

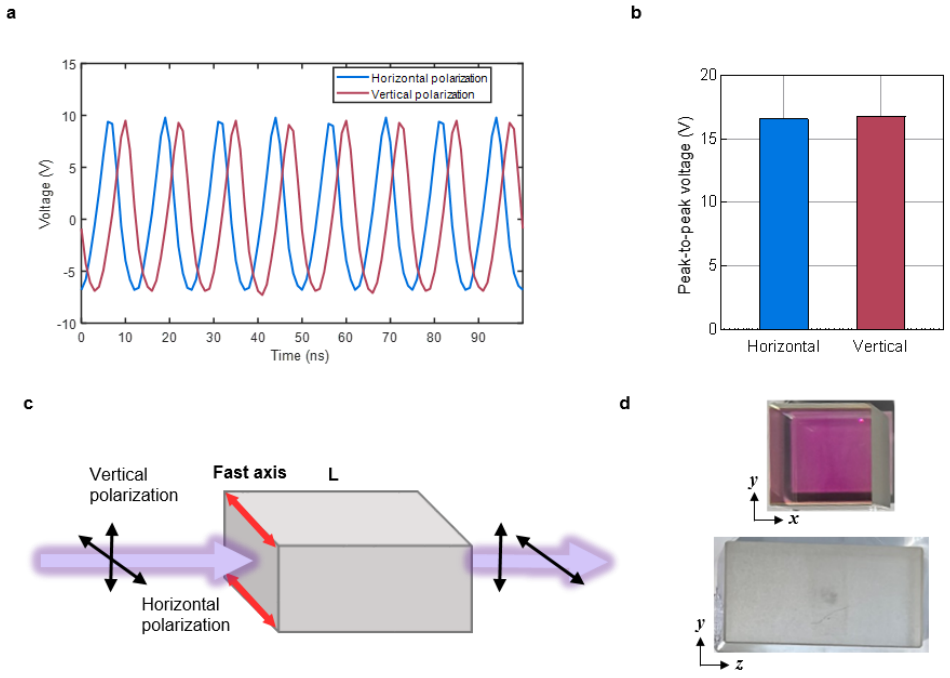

Supplementary Fig. 12 Measured voltages of pump beams and details of BFC design. (**a**) Measured voltages of the two pump beams ($I_{p,H}$ and $I_{p,V}$) detected by the custom dual-channel detector. (**b**) The peak-to-peak voltage of the detected $I_{p,H}$ and $I_{p,V}$. (**c**) BFC design. The optical axis of the BFC was oriented perpendicular to the incident surface and parallel to the bottom edge of the incident surface. (**d**) BFC photos.

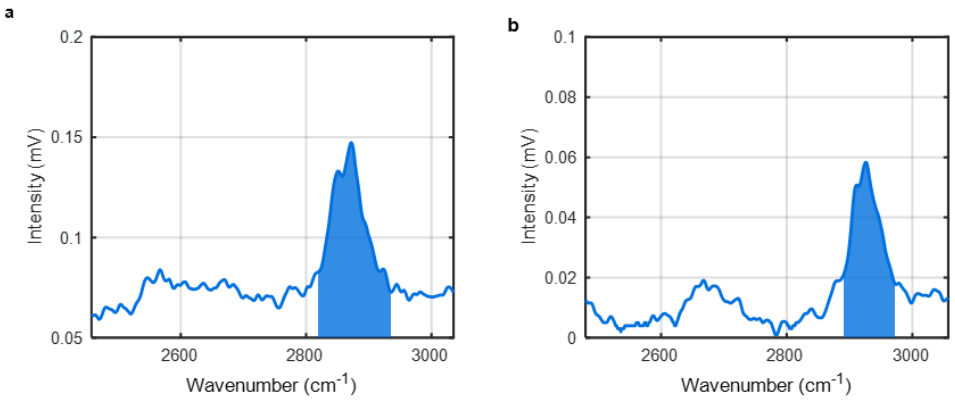

Supplementary Fig. 13 SRS spectrum of CCR8 and PD-1.

The SRS signal of soly CCR8 **(a)** and PD-1 **(b)**. The signal intensity is negligible compared to biological tissues at the therapeutic dosage.

Supplementary Table 1 Comparison of representative fast SRS systems.

Platform	Temporal Resolution	Limitations Compared to SDRSRS
Microsecond spectral-tuning polygon systems[25]	~2–5 μs per step, but full CH-window still requires multi-step tuning	Not simultaneous; requires 20–30 steps for spectral scanning and deep learning
Fast-tuning picosecond fiber-laser SRS[7, 26]	Tens of microseconds to sub-millisecond tuning; dual-color acquisition achieved by rapid wavelength hopping or interleaved pulses	Non-simultaneous acquisition of multiple Raman bands; requires dual-wavelength synchronization hardware; potential temporal mismatch between channels for dynamic samples
Single-shot broadband multiplex SRS[27-30]	Single burst (μs)	Requires multi-channel photodiodes / spectrometer; not easily retrofitted to standard 2P microscopes
Commercial dual color SRS (DC-SRS), e.g., deltaEmerald, APE Inc.	N.A.	Only fixed 85 cm^{-1} energy difference set to address CH_2 & CH_3 at their peak position.
Dual-phase SRS[4]	Simultaneous 2-color	Requires ~4 m of free-space delay lines, sensitive alignment

Supplementary references

1. Hellerer, T., Enejder, A.M.K. & Zumbusch, A. Spectral focusing: High spectral resolution spectroscopy with broad-bandwidth laser pulses. *Appl Phys Lett* **85**, 25-27 (2004).
2. Fu, D., Holtom, G., Freudiger, C., Zhang, X. & Xie, X.S. Hyperspectral imaging with stimulated raman scattering by chirped femtosecond lasers. *J Phys Chem B* **117**, 4634-4640 (2013).
3. Liu, B. et al. Label-free spectroscopic detection of membrane potential using stimulated Raman scattering. *Appl Phys Lett* **106**, 173704 (2015).
4. He, R. et al. Dual-phase stimulated Raman scattering microscopy for real-time two-color imaging. *Optica* **4**, 44-47 (2017).
5. Freudiger, C.W. et al. Label-free biomedical imaging with high sensitivity by stimulated Raman scattering microscopy. *Science* **322**, 1857-1861 (2008).
6. Saar, B.G. et al. Video-rate molecular imaging in vivo with stimulated Raman scattering. *Science* **330**, 1368-1370 (2010).
7. Freudiger, C.W. et al. Stimulated Raman scattering microscopy with a robust fibre laser source. *Nat Photonics* **8**, 153-159 (2014).
8. Fu, D. et al. Imaging the intracellular distribution of tyrosine kinase inhibitors in living cells with quantitative hyperspectral stimulated Raman scattering. *Nature Chemistry* **6**, 615-623 (2014).
9. Cheng, J.-X. & Xie, X.S. Vibrational spectroscopic imaging of living systems: An emerging platform for biology and medicine. *Science* **350**, aaa8870 (2015).
10. Wei, L. et al. Super-multiplex vibrational imaging. *Nature* **544**, 465–470 (2017).
11. Casacio, C.A. et al. Quantum-enhanced nonlinear microscopy. *Nature* **594**, 201–206 (2021).
12. Lin, H. et al. Label-free nanoscopy of cell metabolism by ultrasensitive reweighted visible stimulated Raman scattering. *Nature Methods* (2025).
13. Amend, S.R. et al. Polyploid giant cancer cells: Unrecognized actuators of tumorigenesis, metastasis, and resistance. *The Prostate* **79**, 1489-1497 (2019).
14. Mirzayans, R. et al. Multinucleated giant cancer cells produced in response to ionizing radiation retain viability and replicate their genome. *Int. J. Mol. Sci.* **18**, 360 (2017).
15. Chinen, L.T.D. et al. Circulating polyploid giant cancer cells, a potential prognostic marker in patients with carcinoma. *Int J Mol Sci* **25**, 9841 (2024).
16. Barneda, D. & Christian, M. Lipid droplet growth: regulation of a dynamic organelle. *Current*

Opinion in Cell Biology **47**, 9-15 (2017).

17. Olzmann, J.A. & Carvalho, P. Dynamics and functions of lipid droplets. *Nature reviews. Molecular cell biology* **20**, 137-155 (2019).
18. Kimmel, A.R. & Sztalryd, C. The perilipins: major cytosolic lipid droplet-associated proteins and their roles in cellular lipid storage. *Annual review of nutrition* **36**, 471-509 (2016).
19. Kieu, T.-L.-V. et al. Downregulation of Elovl5 promotes breast cancer metastasis through a lipid-droplet accumulation-mediated induction of TGF-β receptors. *Cell Death Dis* **13**, 758 (2022).
20. Li, Z., Liu, H. & Luo, X. Lipid droplet and its implication in cancer progression. *Am J Cancer Res* **10**, 4112-4122 (2020).
21. Luo, X. et al. Emerging roles of lipid metabolism in cancer metastasis. *Mol Cancer* **16**, 76 (2017).
22. Shen, B.L. et al. Label-free whole-colony imaging and metabolic analysis of metastatic pancreatic cancer by an autoregulating flexible optical system. *Theranostics* **10**, 1849-1860 (2020).
23. Qiu, L. et al. Intratumor graph neural network recovers hidden prognostic value of multi-biomarker spatial heterogeneity. *Nature Communications* **13**, 4250 (2022).
24. Yan, J.S. et al. Monitoring the extracellular matrix remodeling of high-grade serous ovarian cancer with nonlinear optical microscopy. *J Biophotonics* **14**, e202000498 (2021).
25. Lin, H.N. et al. Microsecond fingerprint stimulated Raman spectroscopic imaging by ultrafast tuning and spatial-spectral learning. *Nat Commun* **12**, 3052 (2021).
26. Orringer, D.A. et al. Rapid intraoperative histology of unprocessed surgical specimens via fibre-laser-based stimulated Raman scattering microscopy. *Nat. Biomed. Eng* **1**, 13 (2017).
27. Liao, C.-S. et al. Spectrometer-free vibrational imaging by retrieving stimulated Raman signal from highly scattered photons. *Sci. Adv.* **1**, e1500738 (2015).
28. Berto, P., Scotte, C., Galland, F., Rigneault, H. & de Aguiar, H.B. Programmable single-pixel-based broadband stimulated Raman scattering. *Opt Lett* **42**, 1696-1699 (2017).
29. Liao, C.S. et al. Microsecond scale vibrational spectroscopic imaging by multiplex stimulated Raman scattering microscopy. *Light-Sci. Appl.* **4**, e265 (2015).
30. Czerwinski, L., Nixdorf, J., Di Florio, G. & Gilch, P. Broadband stimulated Raman microscopy with 0.1 ms pixel acquisition time. *Opt Lett* **41**, 3021-3024 (2016).